



Research paper

Structural basis for specific inhibition of salicylate synthase from *Mycobacterium abscessus*

Matteo Mori^{a,1}, Mario Cocorullo^{b,1}, Andrea Tresoldi^a, Giulia Cazzaniga^a, Arianna Gelain^a, Giovanni Stelitano^b, Laurent R. Chiarelli^b, Martina Tomaiuolo^c, Pietro Delre^d, Giuseppe F. Mangiatordi^d, Mariangela Garofalo^e, Alberto Cassetta^c, Sonia Covaceuszach^{c,**}, Stefania Villa^{a,*}, Fiorella Meneghetti^a

^a Department of Pharmaceutical Sciences, University of Milan, Via L. Mangiagalli 25, 20133, Milano, Italy

^b Department of Biology and Biotechnology "Lazzaro Spallanzani", University of Pavia, Via A. Ferrata 9, 27100, Pavia, Italy

^c Institute of Crystallography, National Research Council, Trieste Outstation, Area Science Park – Basovizza, S.S.14 - Km. 163.5, 34149, Trieste, Italy

^d Institute of Crystallography, National Research Council, Via G. Amendola 122/o, 70126, Bari, Italy

^e Department of Pharmaceutical and Pharmacological Sciences, University of Padova, via F. Marzolo 5, 35131, Padova, Italy

ARTICLE INFO

Keywords:

Non-tuberculous mycobacteria
Mycobacterium abscessus
 Siderophores
 Chorismate
 Salicylate synthase
 Inhibition
 Crystal structure
 Cystic fibrosis

ABSTRACT

Blocking iron uptake and metabolism has been emerging as a promising therapeutic strategy for the development of novel antimicrobial compounds. Like all mycobacteria, *M. abscessus* (*Mab*) has evolved several countermeasures to scavenge iron from host carrier proteins, including the production of siderophores, which play a crucial role in these processes. In this study, we solved, for the first time, the crystal structure of *Mab*-SaS, the first enzyme involved in the biosynthesis of siderophores. Moreover, we screened a small, focused library and identified a compound exhibiting a potent inhibitory effect against *Mab*-SaS ($IC_{50} \approx 2 \mu\text{M}$). Its binding mode was investigated by means of Induced Fit Docking simulations, performed on the crystal structure presented herein. Furthermore, cytotoxicity data and pharmacokinetic predictions revealed the safety and drug-likeness of this class of compounds. Finally, the crystallographic data were used to optimize the model for future virtual screening campaigns. Taken together, the findings of our study pave the way for the identification of potent *Mab*-SaS inhibitors, based on both established and unexplored chemotypes.

1. Introduction

M. abscessus (*Mab*), a member of the non-tuberculous mycobacteria (NTM) group, represents a significant and growing global health concern [1–3]. It is the most frequently encountered etiological agent of NTM-related lung conditions, accounting for a vast majority of the total reported cases [4,5]. This opportunistic pathogen can cause chronic pulmonary infections, especially among individuals with pre-existing lung diseases, such as cystic fibrosis (CF) [6–9]. Large-scale epidemiological studies from several countries and regions have reported an alarming prevalence of 3.3–22.6 % in CF patients [10]. Current

chemotherapies require long treatment times, and the clinical outcomes are often disappointing [11,12]. The low level of susceptibility of NTM to a wide range of drugs is attributed to their 'intrinsic' drug resistance, ascribable to their peculiar cell wall, characterized by a large presence of complex lipids, and of several efflux pumps [13,14]. The natural drug resistance of NTM, as well as their ability to form biofilm, lead to severe, treatment-refractory pulmonary infections in susceptible individuals [15]. Therefore, there is an urgent medical need to discover and develop new, more effective anti-NTM drugs [16]. A promising option among innovative solutions to fight antimicrobial resistance is the anti-virulence therapy, which is based on compounds targeting

Abbreviations: %RA, % residual activity; BSA, bovine serum albumin; CF, cystic fibrosis; CNS, central nervous system; DS, docking score; DTT, 1,4-dithio-DL-threitol; IFD, Induced Fit Docking; *Mab*, *Mycobacterium abscessus*; *Mab*-SaS, salicylate synthase from *Mycobacterium abscessus*; *Mtb*, *Mycobacterium tuberculosis*; NTM, non-tuberculous mycobacteria; PDB, Protein Data Bank; QED, Quantitative Estimate of Drug-likeness; RMSD, Root-Mean-Square Deviation; SaS, salicylate synthase.

* Corresponding author.

** Corresponding author.

E-mail addresses: sonia.covaceuszach@ic.cnr.it (S. Covaceuszach), stefania.villa@unimi.it (S. Villa).

¹ These authors contributed equally.

<https://doi.org/10.1016/j.ejmech.2023.116073>

Received 16 November 2023; Received in revised form 15 December 2023; Accepted 17 December 2023

Available online 20 December 2023

0223-5234/© 2023 The Authors. Published by Elsevier Masson SAS. This is an open access article under the CC BY-NC-ND license (<http://creativecommons.org/licenses/by-nc-nd/4.0/>).

pathways that are non-essential for microbial growth but required for pathogenesis [17–19]. Because this approach aims to prevent the attack of a pathogen rather than kill it, anti-virulence compounds do not exert a constant selective pressure, thus preventing resistance phenomena [18, 19]. In this context, considering the importance of iron in sustaining mycobacterial infections, we envisaged to target the uptake and metabolism of this metal for the development of novel antimicrobial compounds against NTM [17]. Notably, their ability to prevent phagosomal maturation inside macrophages was shown to be dependent on iron uptake [5]. Hence, targeting the enzymes that mediate the acquisition of this ion could be an efficient strategy to inhibit bacterial virulence [20]. Although innate host defense strategies induce the restriction of essential nutrients during the infection, *Mab*, along with other mycobacterial species, has evolved several countermeasures to scavenge iron from carrier proteins [21–24]. The production of siderophores, namely the hydrosoluble carboxymycobactin and the lipophilic mycobactin, plays a crucial role in these processes [20,24,25]. Their biosynthesis has been widely studied in *M. tuberculosis* (*Mtb*) [23], but it has never been considered in NTM. However, in light of the phylogenetic relatedness between these species, similar functional and mechanistic roles are likely. Therefore, in analogy with the *Mtb* system, the enzymes involved in the biosynthesis of *Mab* siderophores may become potential drug targets [20]. The first player in this pathway is a salicylate synthase (SaS, known as MbtI in *Mtb*) that converts chorismic acid to salicylic acid. *Mab*-SaS does not have any counterpart in human cells, thus being an ideal target for the development of safe antimycobacterial drugs [26].

In our previous work, we first approached the study of this enzyme and identified effective inhibitors based on the 5-phenylfuran-2-carboxylic acid structure, which has emerged in the past years as a promising and safe scaffold for targeting MbtI [27]. Their activity was rationalized by means of molecular docking simulations, performed using a homology model developed *ad hoc* by our group and generated from the coordinates of MbtI in complex with a member of this compound class (PDB_ID: 6ZA4 [28]) [20]. Among the most interesting candidates, **I** (Fig. 1) emerged as the most potent, with an IC_{50} of about 5 μ M [20].

To support our structure-based drug design efforts and obtain an experimental model for further (and even more reliable) computational studies, we decided to perform crystallographic investigations. Herein, we report the results of our endeavors, which led to the first-ever crystal structure of *Mab*-SaS. Our crystallographic analysis revealed that the

overall enzyme architecture was remarkably similar to that of MbtI, especially in the active site cleft. This was especially important to support the validity of our inhibitor-discovery approach, based on adopting the 5-phenylfuran scaffold, which has been demonstrated to be promising for MbtI inhibition. Nevertheless, despite a general conservation of the key residues, we identified differences that could likely impact on the ability of different chemical moieties to enter the binding pocket, thus differentiating *Mab*-SaS from MbtI in its ability to bind ligands [20].

With this premise, we expanded our panel of inhibitors by screening a focused library of *m*-substituted 5-phenylfuran-2-carboxylic acid derivatives. This biochemical investigation was instrumental in selecting a new inhibitor, exhibiting an improved activity against *Mab*-SaS. The importance of its main pharmacophore features was verified by a specifically conceived small collection of molecules. Overall, the functional results confirmed the existence of differences between the effect of the compounds on the two SaSs from *Mtb* and *Mab*. Therefore, we analyzed our data in light of the new crystal structure, rationalizing the activity of our compounds by a thorough computational evaluation. Our in-silico studies also included investigations on the drug-likeness and pharmacokinetic properties of the compounds.

Taken together, the crystallographic and computational data allowed us to examine the molecular basis of *Mab*-SaS inhibition, paving the way for the optimization of the promising 5-phenylfuran-2-carboxylic acid-based compounds, as well as for future virtual screening campaigns. The body of information gathered in this work will hopefully lead to relevant therapeutic advances in the treatment of *Mab* infections, alleviating the burden on CF patients.

2. Results and discussion

2.1. Crystallographic structure of *Mab*-SaS

The structural characterization of pharmacological targets is crucial for the development of enzymatic inhibitors as potential drugs. Therefore, to open novel therapeutic avenues for the treatment of *Mab* infections in CF patients, we approached the study of *Mab*-SaS, a previously unexplored target involved in the acquisition of iron [20]. *Mab*-SaS belongs to the family of the Chorismate-Utilizing Enzymes, and more specifically to the Menaquinone, Siderophore, Tryptophan subclass [29,30]. Considering the well-known plasticity of the active site of

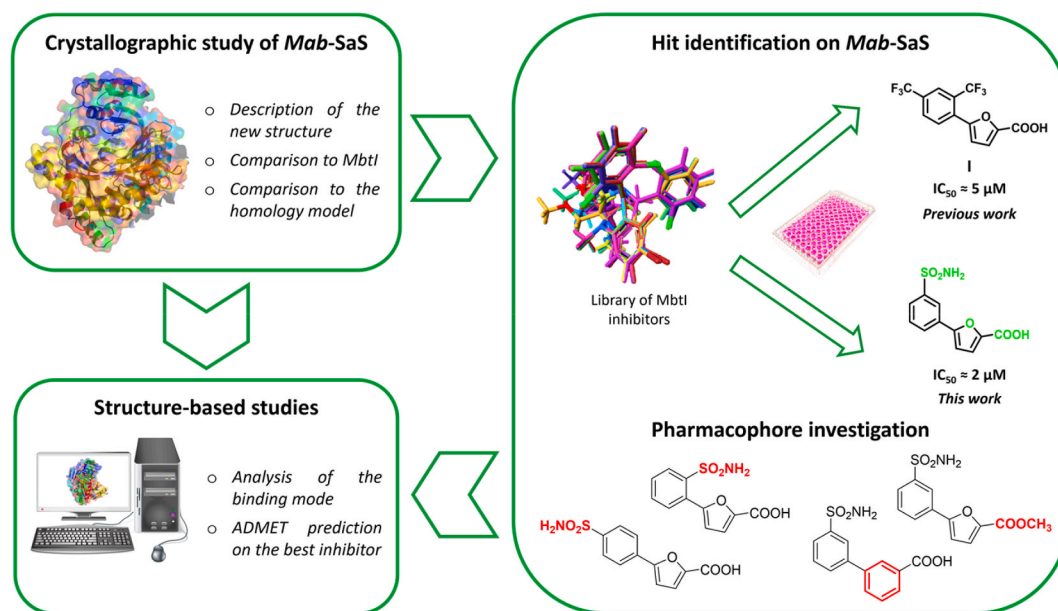


Fig. 1. Process diagram of the work presented in this paper, encompassing crystallographic investigations on *Mab*-SaS, the identification of potent enzymatic inhibitors, and computational studies.

these proteins [31], structural investigations are always very informative for the design of ligands. In our previous work, we identified the first enzymatic inhibitors of *Mab*-SaS (compound I, Fig. 1) and studied their interaction within the binding pocket by means of computational investigations on a homology model, based on the coordinates of the *Mtb* congener MbtI (PDB_ID: 6ZA4 [28]), which is a very close ortholog of *Mab*-SaS (Fig. S22) [20]. Herein, we present the results of our efforts, which were rewarded with the first crystal structure of *Mab*-SaS, solved at 2.07 Å resolution. Our data provided atomic-level information on the binding pocket, allowing the identification of the key amino acid residues available for the binding of ligands.

The crystal structure was successfully refined in the orthorhombic P2₁2₁2₁ space group, showing overall good quality indicators and a sound geometry. A continuous electron density map was observed, spanning from residue 17 to residue 452 for both molecules within the asymmetric unit. However, areas of weaker electron density were observed in the N-terminal (A22-27, C27) and C-terminal regions (A452, C452), in portions forming turns (C81), and in the C-term of helix α3 (C170-172), as illustrated in Fig. S22. It is noteworthy that the two molecules (chains A and C) exhibited nearly identical conformations, with a Root-Mean-Square Deviation (RMSD) of 0.432 Å, calculated over 432 Cα atoms (Fig. S23). Some disparities between the two chains were detected in regions 20–30, 73–93, and 148–152, suggesting a higher flexibility.

The analysis of the crystallographic dimer indicated that it was likely a consequence of the crystallization process and lacked any functional significance. This notion was confirmed by the results of a PISA [32] analysis of the interaction surfaces and further substantiated by size-exclusion chromatography, which revealed a single peak, consistent with a monomeric state.

Due to the monomeric nature of the enzyme and the high structural similarity between the two molecules in the asymmetric unit, the subsequent discussion is based on the analysis of chain A. The overall topology of *Mab*-SaS was similar to that of MbtI (see Fig. S24) and other enzymes or domains exhibiting salicylate synthase activity [33]. In detail, it was characterized by two α/β subdomains, each comprising two large antiparallel β-sheets with 10 and 11 strands, tightly packed in an almost orthogonal manner and flanked by α-helices (Fig. 2A). The

active site was situated in a cleft delimited by helices α7, α10, and η4, as well as by β-strands β14, β17, and β21, consistent with the arrangement observed in MbtI and homologous enzymes. Significant structural congruence with MbtI was observed in the active site cleft, particularly in the region encompassing residues K207, Y387, R407, and K440, which have been identified as crucial for the catalytic activity [33] and have also been linked to the inhibition of the enzyme [28,34]. In this regard, the binding pocket is generally well-conserved among chorismate-utilizing enzymes, like salicylate synthase from *Y. enterocolitica* (Trp9, PDB_ID: 2FN0) [35], anthranilate synthase from *S. marcescens* (TrpE, PDB_ID: 1I7Q) [36], and aminodeoxychorismate synthase from *E. coli* (PabB, PDB_ID:1K0G) [37]. Despite their different biosynthetic role and lower degree of sequence identity, which can be as low as ~20 %, key residues are mostly conserved and adopt almost identical geometries. For these enzymes, few differences are observed in the binding pocket; some examples are K207, which is found as a glutamine in both PabB and TrpE, E296, which is an aspartate in PabB, and Y387, which is a tryptophan in PabB. However, despite their different chemical nature, all of them share the same spatial orientation. For all the enzymes here described with exception of PabB, glutamate residues involved in Mg²⁺ coordination are strictly conserved, likely due to the relevance of Mg²⁺ for their catalytic activity. A comparison of the crystallographic structures of these chorismate-utilizing enzymes shows that the side chains of the glutamate residues involved in Mg²⁺ coordination may collectively adopt two different orientations, depending on the presence of the bivalent ion in the crystallization cocktail. The rather strict conservation of the binding pocket topology supports the validity of our inhibitor-discovery approach, based on adopting the 5-phenylfuran scaffold, which has been demonstrated to be promising for MbtI inhibition. The main structural differences between *Mab*-SaS and MbtI were detected in the N-terminal region, which is the most variable in all enzymes belonging to this class. Furthermore, despite the remarkable conservation of the binding pocket, a MOLE [38] analysis revealed that the active site in *Mab*-SaS encompassed a solvent accessible channel ≈ 27 Å-long (Fig. 2B), which was remarkably shorter than that of MbtI (≈41 Å) and different in terms of electrostatic properties (Fig. 2C). Moreover, we identified two key residues at the entrance of the active-site cleft, namely A427 and T429, corresponding to E425 and

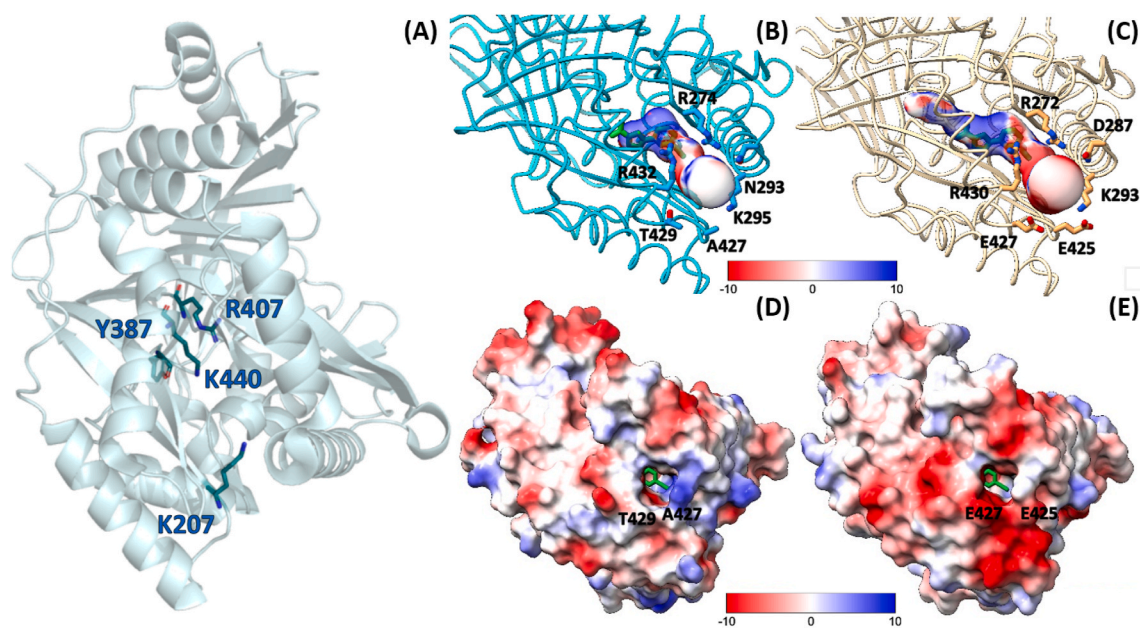


Fig. 2. Molecular structure of *Mab*-SaS: the protein is portrayed as a cartoon diagram, with selected residues highlighted as green sticks (A); volumetric representation of the active-site cleft channels in *Mab*-SaS (B) and MbtI (PDB_ID: 3LOG) (C), colored according to the local electrostatic potential; electrostatic potential (kT units) at the protein surface (represented as Solvent Accessible Surface, SAS) in *Mab*-SaS (D) and MbtI (PDB_ID: 3LOG) (E) with the inhibitor M83 (1k in this work) represented as green sticks, as determined in the MbtI-inhibited crystal structure (PDB_ID: 6ZA4).

E427 in MbtI, with a significant impact on the electrostatic potential of this region (Fig. 2D and E). These relevant discrepancies can be expected to influence the ability of different chemical moieties to enter the binding pocket, thus discriminating *Mab*-SaS from MbtI in its ability to bind ligands, including 5-phenylfuran-2-carboxylic acid derivatives.

The crystallization conditions employed in this study led *Mab*-SaS to adopt a "closed-form" conformation, much like MbtI in some crystal structures available in the literature (e.g., PDB_ID: 3LOG [39]) [28,34]. The RMSD deviation between our *Mab*-SaS model and the closed form of MbtI (PDB ID: 3LOG) was calculated to be 0.837 Å, upon alignment of 428 C α atoms. The difference between the closed and open forms in MbtI has been attributed to the movement of specific regions of the enzyme, including residues 268–293 and 324–336, which are highly conserved in *Mab*-SaS. Like MbtI, the closed form of *Mab*-SaS was primarily characterized by the closer positioning of β 14, α 6, β 15, and β 16 relative to α 10 and β 21, located on opposite faces of the cleft. The absence of bulky inhibitors or reaction products, as well as the presence of oxyanions in the crystallization solution, likely favored and stabilized *Mab*-SaS in the closed form, akin to inhibitor-free MbtI. In detail, two sulfate ions, supplied in the crystallization condition, were identified within the catalytic cleft, occupying positions typically held by oxyanions or carboxylate moieties in salicylate synthase structures [28,33,34] (Fig. S25). The first sulfate ion was deeply nestled in the catalytic cleft and formed hydrogen bonds with Y387 ($^{387}\text{OH}\cdots^{506}\text{O4}$, 2.3 Å), while engaging in a salt bridge with R407 ($^{407}\text{N}\eta 2\cdots^{506}\text{O4}$, 3.2 Å; $^{407}\text{Ne}\cdots^{506}\text{O3}$, 3.0 Å). An ionic interaction was also established with K440 ($^{440}\text{N}\zeta\cdots^{506}\text{O1}$, 3.0 Å), accompanied by an additional hydrogen bond with G421 ($^{421}\text{N}\cdots^{506}\text{O2}$, 2.7 Å). The second sulfate ion occupied a region that typically accommodates oxyanions or the carboxylic group of the salicylate moieties in MbtI structures [28,34]. This sulfate ion was engaged in hydrogen bonds with G423 ($^{423}\text{N}\cdots^{503}\text{O2}$, 3.1 Å), G272 ($^{272}\text{N}\cdots^{503}\text{O3}$, 2.7 Å), and T273 ($^{273}\text{O}\gamma\cdots^{503}\text{O3}$, 3.1 Å) and K440 ($^{440}\text{N}\zeta\cdots^{503}\text{O4}$, 3.3 Å), while also participating in a water network. This sulfate ion played a pivotal role in stabilizing the closed-form conformation of the enzyme by bridging G423 on β 21, G272, and T273 on β 14, thus restricting the conformational flexibility in the active-site cleft. Furthermore, several water molecules mediated interactions between the sulfate ion and residues located in the pocket, including K207, whose importance in catalysis has been well-established. Notably, the closed form adopted by *Mab*-SaS appeared to be independent of the presence of bivalent positive counterions, although the possibility of Na⁺ ions cannot be entirely ruled out. It is worth noting that this closed-form conformation may hamper the binding of 5-phenylfuran-2-carboxylic acid derivatives in the catalytic cleft. In this respect, we carried out a DynDom [40] analysis on MbtI, studying the protein flexibility and

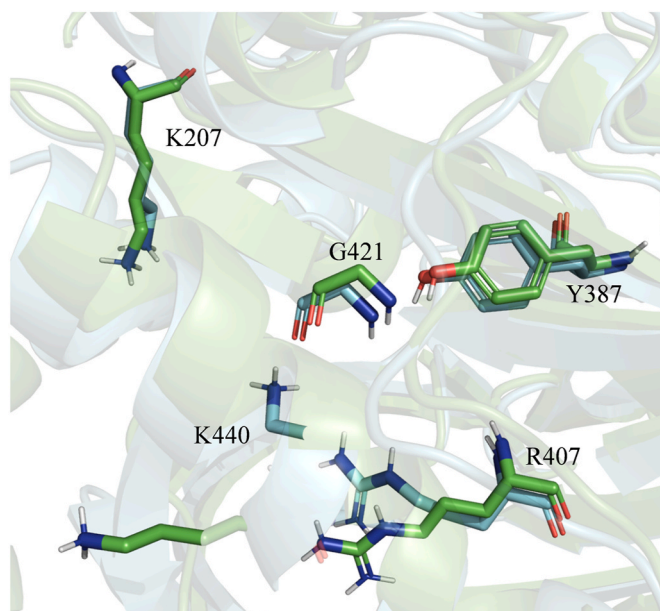


Fig. 3. Structural superimposition between the homology model of *Mab*-SaS (green) and its crystal structure (blue). Important residues are rendered as sticks and the protein as cartoon.

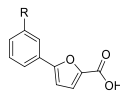
rigid-body domain movements upon ligand binding. We compared the inhibited and inhibitor-free MbtI crystal structures (PDB_ID: 6ZA4 and 3LOG), assuming an open and closed conformation respectively, highlighting the existence of two rigid domains rotating and shifting of $\approx 6^\circ$ and ≈ 1 Å upon inhibitor binding (Fig. S5, Table S1). It is noteworthy that residues 319–322 and 340–343 (319–322 and 340–343 in *Mab*-SaS), which are part of a flexible region critical for the movement of these domains, display a low conservation in *Mab*-SaS (Fig. S1, Table S2) and might have a substantial effect on the ability of *Mab*-SaS to assume an open conformation.

Incidentally, the role of sulfate ions in stabilizing the closed conformation of *Mab*-SaS underlines not only the potential influence of the crystallization environment on the structural state of the enzyme, but also its propensity to interact with molecules bearing $-\text{RSO}_2$ groups, as confirmed by the biological tests on compounds **1h** and **1i** (see the following section and Table 1).

To compare the binding site of the recently employed homology model [20] with the X-ray structure of *Mab*-SaS presented in this study, we conducted a superimposition of the two protein structures, followed

Table 1

In vitro activity of the *m*-substituted derivatives **1a**–**1k** on *Mab*-SaS and *Mtb*-MbtI, expressed as % of residual enzymatic activity at 100 μM (%RA) and half maximal inhibitory concentration (IC_{50}). IC_{50} values were measured for compounds showing %RA < 30.



Entry	R	% RA (<i>Mab</i> -SaS)	IC_{50} (μM) (<i>Mab</i> -SaS)	% RA (<i>Mtb</i> -MbtI)	IC_{50} (μM) (<i>Mtb</i> -MbtI)
1a	CF ₃	35.0 \pm 5.9	–	42.0 \pm 6.3	–
1b	Cl	88.3 \pm 5.9	–	101.6 \pm 17.8	–
1c	OH	65.0 \pm 2.4	–	70.4 \pm 21.8	–
1d	CH ₃	54.7 \pm 4.5	–	103.9 \pm 4.8	–
1e	NH ₂	48.3 \pm 5.2	–	65.8 \pm 9.6	–
1f	CONH ₂	25.8 \pm 3.2	42.9 \pm 3.9	20.9 \pm 4.3	31.4 \pm 10.3
1g	CONHCH ₃	53.3 \pm 5.9	–	84.0 \pm 9.1	–
1h	SO ₂ NH ₂	0.6 \pm 0.5	2.6 \pm 1.1	28.6 \pm 6.8	39.7 \pm 5.9
1i	SO ₂ CH ₃	5.4 \pm 3.0	3.6 \pm 0.4	25.8 \pm 1.0	34.9 \pm 3.7
1j	COOH	33.3 \pm 2.5	–	27.2 \pm 4.5	35.2 \pm 2.6
1k	CN	3.2 \pm 2.1	12.1 \pm 1.1	3.1 \pm 1.0	6.3 \pm 0.9

by a preliminary visual inspection. Our specific focus was on three critical amino acids, namely Y387, G421, and K207, which are known to play a pivotal role in molecular recognition [20]. It is noteworthy that the side chain conformation of these residues exhibited a high degree of similarity, as supported by the relative RMSD value (0.58 Å for Y387; 0.61 Å for G421; 1.62 Å for K207). Conversely, a notable disparity emerged when we examined the side chains of K440 (RMSD = 9.87 Å) and R407 (RMSD = 3.78 Å). These residues are situated within the cavity and in close proximity to Y387, G421, and K207. In contrast to the homology model, the crystal structure revealed that the side chains of both K440 and R407 were oriented within the binding site. This positioning suggests a potential hindrance to the accommodation of ligands within the cavity, as illustrated in Fig. 3.

2.2. Identification, synthesis, and biological activity of *Mab-SaS* inhibitors

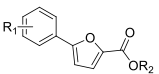
In our ongoing attempts to discover new compounds acting on *Mab-SaS*, we focused on *m*-substituted 5-phenylfuran-2-carboxylic acid derivatives (1a-k, Table 1). This subclass of analogs had performed well on MbtI and included the lead-inhibitor 5-(3-cyanophenyl)furan-2-carboxylic acid. However, our previous screening had also hinted at discrepancies between the biological effects of the compounds on the two SaSs; these differences were rationalized here by the analysis of the crystallographic structure of *Mab-SaS* in comparison to MbtI. On this basis, we chose to test all the *m*-substituted analogs at our disposal, irrespective of their performance on the *Mtb* ortholog. According to our results, compound 1h proved to be the most effective against *Mab-SaS*, with an IC₅₀ value in the low micromolar range (Table 1).

Therefore, 1h was subjected to further analyses to ascertain that it did not act as a PAIN compound [41]. Our tests confirmed that, indeed, 1h did not behave as a PAIN; as shown in Fig. S27, its IC₅₀ in the presence of BSA (2.8 ± 0.48 μM) or Triton X-100 (2.8 ± 0.48 μM) did not differ significantly from the previously obtained value (Table 1). Finally, to exclude a promiscuous enzyme inhibition due to covalent reaction with cysteines, the activity was also tested in the presence of 100 μM DTT. Again, the IC₅₀ was not influenced by the reducing reagent (3.3 ± 0.66 μM), thus excluding an unspecific interaction of 1h with the cysteine residues of *Mab-SaS*.

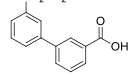
Compared to 1h, the amide derivative 1f showed a reduced activity. Conversely, the insertion of a methyl sulfonyl moiety (1i) led to a retention of the inhibitory effect, supporting the importance of the -RSO₂ group in the interaction with the enzyme. Most notably, 1k exhibited a higher IC₅₀ compared to MbtI, further confirming our initial observations of slight but meaningful differences in the activity of the inhibitors on the two enzymes. All other compounds showed poor-to-negligible effects. Overall, our results indicated that *Mab-SaS* was more sensitive to variations in the nature of the *m*-substituent with respect to its *Mtb* homolog.

To better characterize the new lead 1h and assess the importance of its pharmacophore features, we performed a SAR study on a small

Table 2
In vitro activity (%RA, IC₅₀) of derivatives 2–5 on *Mab-SaS*.



Entry	R ₁	R ₂	% RA [†]	IC ₅₀ (μM) [†]
2	4-SO ₂ NH ₂	H	16.0 ± 6.5	19.3 ± 1.7
3	2-SO ₂ NH ₂	H	97.1 ± 13.5	–
4	3-SO ₂ NH ₂	CH ₃	55.3 ± 12.4	–
5	SO ₂ NH ₂		89.4 ± 13.8	–



collection of derivatives (2–5, Table 2). Initially, we verified the importance of the *meta* position (2,3), then we evaluated the effect of alternatively removing the carboxylic acid (4) and the furan ring (5). As shown in Table 2, we found that moving the sulfonamide group to the *para* position (2) allowed for a partial retention of the activity, leading to an IC₅₀ of 19.3 μM. Conversely, when the same group was inserted at the *ortho* position (3), we observed a complete abolishment of the inhibitory effect. The masking of the carboxylic moiety in 4 with an ester function led to a considerable loss in the activity, probably due to the increased steric hindrance and the disruption of the hydrogen bond network involving the acid. Moreover, we cannot exclude that the limited activity shown by the compound could be due to a partial hydrolysis of the relatively weak methyl ester in the assay conditions. Finally, the removal of the furan and its replacement by a simple phenyl ring (5) suppressed the inhibitory effect, confirming the essentiality of the heterocycle.

Overall, these biological results demonstrated that our scaffold is suitable to gain a potent inhibition of *Mab-SaS*. The main pharmacophore features are the furan ring, which was also proven to be the best heterocycle for the targeting of MbtI, and a hydrogen bond acceptor at position 2, with the carboxylic moiety being the most efficient. Modifications to the phenyl ring at position 5 of the furan modulate the biological profile of the compounds; here, we discovered that the *m*-SO₂NH₂ substitution offers the possibility to achieve the best results in terms of enzyme inhibition, compared to other functional groups.

Compounds 1a-h,j-k and 2 were prepared according to the procedures detailed in our previous works [28,42]. The new derivatives 1i, 3, and 4 (published as an intermediate in Ref. [28]) were synthesized with the same approach (Scheme 1). Briefly, (5-(methoxycarbonyl)furan-2-yl)boronic acid was reacted in a Suzuki–Miyaura cross-coupling with a properly substituted bromobenzene (6–8), affording the key ester intermediates (4, 9, 10), which were hydrolyzed to the final carboxylic acids (1i and 3) in basic conditions.

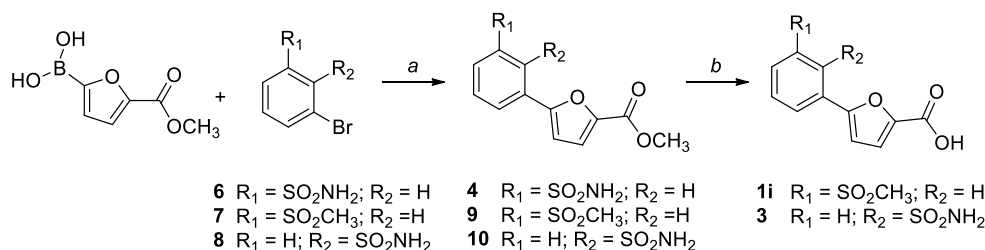
Compound 5 was obtained in a similar fashion, as illustrated in Scheme 2. Methyl 3-bromobenzoate was converted to its boron pinacolate derivative (11) with bis(pinacolato)diboron in the presence of [1,1'-bis(diphenylphosphino)ferrocene]dichloropalladium(II). Then, 11 was reacted with 3-bromobenzenesulfonamide (6) in a Suzuki coupling to give intermediate 12, which was hydrolyzed to the corresponding acid (5) with lithium hydroxide. Further synthetic details are discussed in the Materials and Methods section.

2.3. Cytotoxicity studies

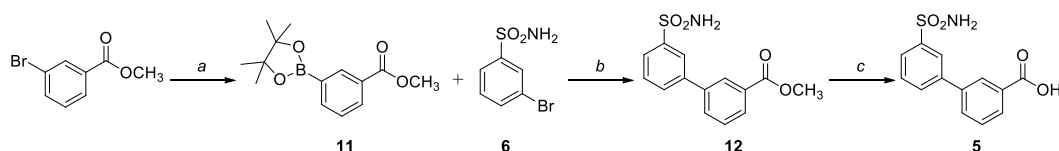
5-Phenylfuran-2-carboxylic acid derivatives have been demonstrated to be non-toxic to several mammalian cells, including murine alveolar-like macrophage MPI-2 [43] and human MRC-5 fibroblast [44], as well as to human platelets, red blood cells, and white blood cells [43], even at relatively high doses. Nevertheless, to further verify the safety of this class, we decided to test the best compound of series (1h) on juvenile fibroblasts, isolated from human male foreskin. As expected, 1h did not show significant cytotoxic effects, with 99.5 % of viable cells in the presence of the highest tested concentration (10 μM, corresponding to ≈ 5 times the IC₅₀; Fig. S28). Further information is available in the Materials and Methods section.

2.4. Molecular modelling

To provide a molecular rationale for the observed experimental data, we investigated the four most active derivatives, namely 1f, 1h, 1i, and 1k (Table 1). Fig. 4 shows the top-scored docking poses returned by the IFD simulations. All the studied derivatives were predicted to share a similar binding mode, primarily driven by hydrogen bond interactions. Specifically, molecular recognition was attributed to:



Scheme 1. Reagents and conditions: a) Pd(PPh₃)₂Cl₂, 2 M Na₂CO₃, 1,4-dioxane, 60 °C, 70 min, MW, N₂; b) LiOH·H₂O, THF/H₂O 2:1, RT, 4 h.



Scheme 2. Reagents and conditions: a) [(dppf)PdCl₂], B₂Pin₂, KOAc, DME, 100 °C, 25 min, MW, N₂; b) Pd(PPh₃)₂Cl₂, 2 M Na₂CO₃, 1,4-dioxane, 60 °C, 70 min, MW, N₂; c) LiOH·H₂O, THF/H₂O 2:1, RT, 6 h.

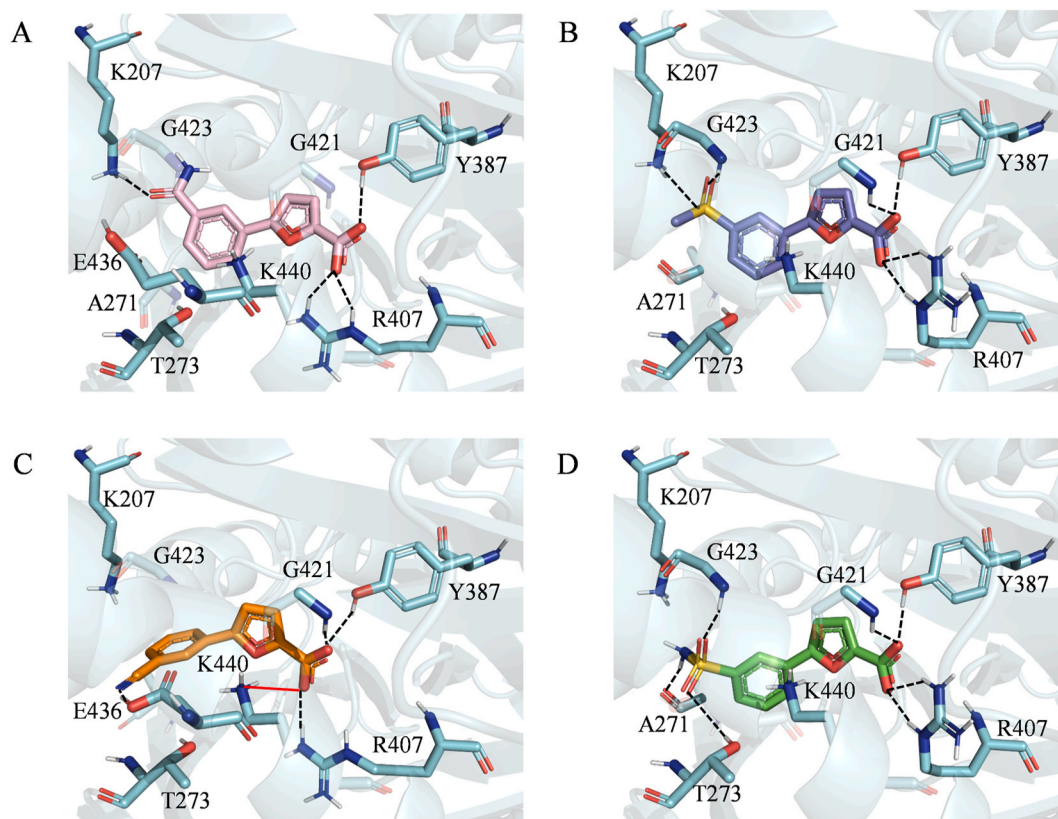


Fig. 4. Top-scored docking poses returned by docking simulations performed on **1f** (A), **1i** (B), **1k** (C) and **1h** (D) within the binding site of Mab-SaS (PDB_ID: 8QLJ). Ligands and important residues are rendered as sticks, the protein as cartoon. The H-bond interactions are itemized by a black dashed line. Salt bridge and cation- π interactions are depicted as red and green lines, respectively. For the sake of clarity, only polar hydrogen atoms are shown.

- i) several well-oriented hydrogen bond interactions, established by the carboxylate moieties of the compounds and R407, Y387, and G421 (except for **1f**);
- ii) a cation- π (salt bridge) interaction between the furan ring of **1h** and K440 (the same interaction was predicted to be established by the carboxylate moiety of **1f**);
- iii) additional hydrogen bond interactions depending on the substituent of the phenyl moiety.

As shown in Fig. 4, the presence of the sulfonamide group (**1h**), which was experimentally associated with the best biological activity, facilitated the formation of additional hydrogen bond interactions, involving the backbones of G423 and A271, as well as the side chain of T273. The contact with G423 was retained by **1i**, which, in turn, formed a hydrogen bond with K207. When the SO₂ was replaced by a C=O (**1f**), the H-bond interaction with G423 could not be established. This provided a possible rationale behind the reduced activity of these compounds. Notably, the cyano group of **1k** formed a hydrogen bond with

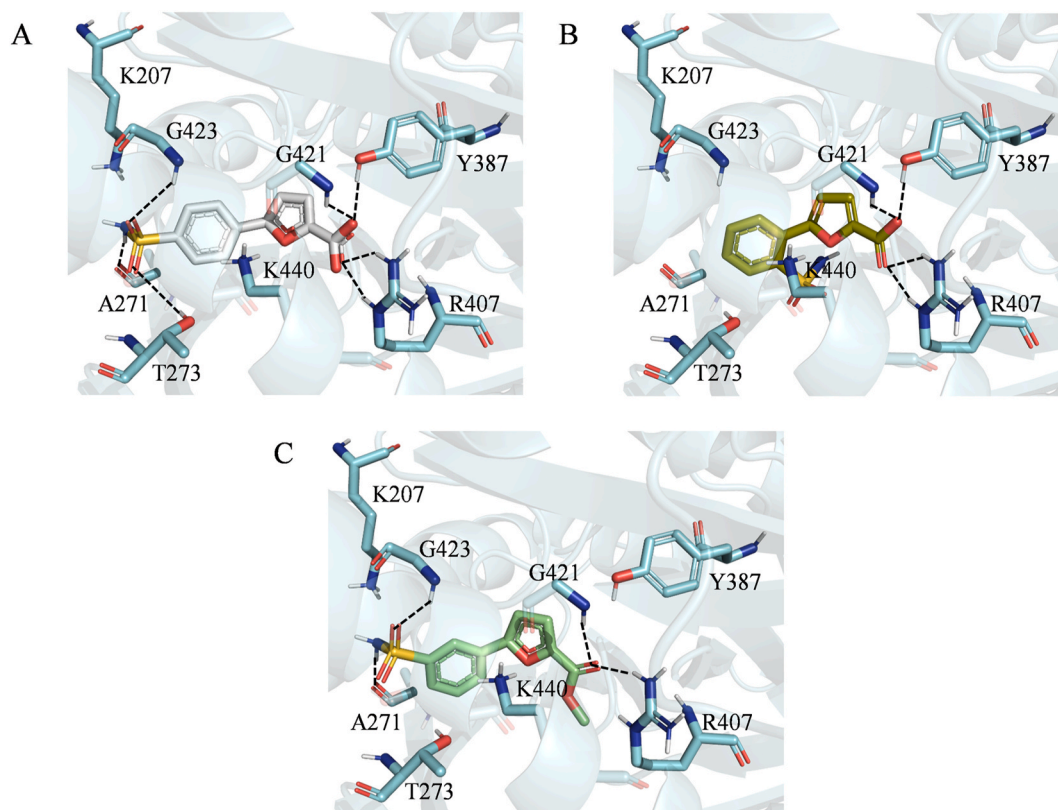


Fig. 5. Top-scored docking poses returned by docking simulations performed on **2** (A), **3** (B) and **4** (C) within the binding site of *Mab-SaS* (PDB_ID: 8QIJ). Ligands and important residues are rendered as sticks, the protein as cartoon. The H-bond interactions are itemized by a black dashed line. Salt bridge and cation- π interactions are depicted as red and green lines, respectively. For the sake of clarity, only polar hydrogen atoms are shown.

E436, in striking contrast to the **1k**-MbtI complex (PDB_ID: 6ZA4 [28]), where the same group was proved to establish an interaction with K205 (here K207). Furthermore, the computed scores aligned well with the experimentally measured activity data, with the docking score (DS) for **1h** better than those calculated for **1f,i,k**. To provide specific values, the docking score (DS) for **1h** was -8.97 kcal/mol, resulting in a calculated binding free energy (ΔG) of -37.30 kcal/mol. In comparison, the DS for **1f** was -8.48 kcal/mol ($\Delta G = -37.07$ kcal/mol), for **1i** -7.83 kcal/mol ($\Delta G = -37.04$), and finally for **1k** -7.06 kcal/mol ($\Delta G = -31.06$ kcal/mol).

The binding mode of compounds **2–5** was also investigated by means of molecular docking simulations to provide a possible explanation behind the importance of the SO_2NH_2 substituent at position 3. In detail, we performed these studies using the protein conformation returned by the IFD simulations on **1h** (see the Materials and Methods section for further information).

In agreement with the experimental data, **2** returned the best docking score (-7.83 kcal/mol, the interested reader is referred to [Table S1](#), available in the Supplementary Materials, for all the computed docking

scores). As expected, a binding mode close to that already observed for **1h** was predicted by our simulations. More specifically, the carboxylate moiety established hydrogen bonds with R407, Y387, and G421 (as depicted in [Fig. 5](#)). Notably, the relocation of the sulfonamide group from position 3 to position 4 on the phenyl ring did not impact on its interaction pattern, which remained unaltered with respect to that of **1h**. On the contrary, moving the sulfonamide group from position 3 to position 2 (**3**) and replacing the carboxylate moiety with an ester function (**4**) disrupted the formation of several hydrogen bonds. Specifically, compound **3** lost the hydrogen bond interactions with G423, A271, and T273, while compound **4** could not contact Y387. Most notably, the position of one of the sulfate ions embedded in the crystal structure well overlapped with that predicted for the 3-sulfonamide group by the docking simulations, thus further supporting the reliability of the employed computational protocol. Interestingly, the docking scores seemed to be significantly affected by the number and strength of the hydrogen bond interactions formed with critical residues within the binding site (*i.e.*, Y387 and R407), showing a clear relationship with the experimentally measured activity data. In detail,

Table 3

Drug-likeness and pharmacokinetic properties computed for the compounds under investigation. Notice that the QED values were obtained by using an in-house script based on the paper by Bickerton et al., while the software program QikProp, available from the Schrodinger suite 2022-4, was employed to compute all the other relevant ADME properties.

Entry	QED	CNS	Human Oral Absorption	Human Oral Absorption (%)	Rule of Three
1f	0.85	-2	2	54.51	1
1h	0.80	-2	2	45.88	1
1i	0.83	-2	3	61.52	0
1k	0.80	-2	3	65.68	0
2	0.80	-2	2	45.67	1

compounds that formed well-oriented hydrogen bonds with these residues showed enhanced *in vitro* inhibitory activity towards *Mab-SaS*, underscoring the significance of the carboxylate moiety. Moreover, specific substituents on the phenyl ring were predicted to contribute to the measured affinity by establishing additional interactions with G423, K207, A271, and T273. Taken as a whole, these data support the idea whereby the crystal structure presented herein, combined with a robust docking protocol, can be a valuable starting point for the rational design of molecules targeting *Mab-SaS*. More specifically, docking simulations could be effectively performed using a model based on the protein conformation generated by the IFD simulations carried out on **1h** (which we made available as supplementary material).

2.5. *In-silico* pharmacokinetics and cardiotoxicity evaluation

Given the importance of having pharmacokinetics predictions from the beginning of the drug design stage, the most interesting compounds belonging to our series (**1f**, **1h**, **1i**, **1k**, and **2**) were also subjected to an *in-silico* evaluation of their pharmacokinetics, today considered of utmost importance for maximizing the rate of success of a drug discovery program [45]. As a first step, we calculated the Quantitative Estimate of Drug-likeness (QED), which is a commonly used integrated score for estimating the drug-likeness of a given small molecule [46]. Generally, promising drug candidates are supposed to return a QED value greater than 0.6. The results of this analysis are presented in Table 3. Importantly, all the compounds under evaluation returned a $QED \geq 0.80$, as a strong indication of their excellent drug-likeness.

It is well known that a drug designed to treat *Mab* infections should not be active in the Central Nervous System (CNS), considering the extreme rarity of a CNS involvement in *Mab*-related conditions [47], differently from *Mtb* [48]. With this in mind, we also assessed several descriptors related to CNS activity and oral adsorption in humans, using the software QikProp [49]. These descriptors included:

- (i) CNS: provides an estimation of CNS activity on a scale from -2 (inactive) to $+2$ (active).
- (ii) Human Oral Absorption: provides a score indicating low (1), medium (2), or high (3) qualitative human oral absorption.
- (iii) Percent Human Oral Absorption: offers a score on a scale from 0 to 100 %, with values above 80 % considered high and values below 25 % regarded as poor.
- (iv) Rule Of Three: represents the number of violations of the Jorgensen's "rule of three" [50], where compounds with no violations are expected to be orally available.

As shown in Table 3, all the compounds were predicted to be inactive on the CNS and with a good oral absorption, with **1i** and **1k** returning the best values. Furthermore, we also assessed the metabolic liability of our compounds by studying their ability to interact with specific cytochrome P450 isoforms, such as CYP1A2, CYP2A6, CYP2B6, CYP2C8, CYP2C9, CYP2C19, CYP2D6, CYP2E1, and CYP3A4. To make these predictions, we employed the CypReact software, a tool developed by Tian et al. [51], and available in the recently published web platform for de-novo design DeLA-Drug [52]. Interestingly, all the compounds were predicted not to be substrates of P450 isoforms, with the only exception of **1k** (possible reaction with CYP1A2 only).

We finally performed an *in-silico* evaluation of the cardiotoxic potential of our compounds. Notice that cardiotoxicity, usually due to off-target interactions with the cardiac Human-Ether-a-go-go-Related (hERG) potassium channel, is today recognized as a common side effect of drugs in clinical phases or under post-market surveillance [53]. More specifically, it is acknowledged that evaluating this endpoint is of utmost importance in the context of *M. abscessus* treatment. To the best of our knowledge, most of the drugs currently recommended for the treatment of this infection (*i.e.*, clarithromycin, azithromycin, and clofazimine) are known to be hERG channel blockers [54]. Hence, a

recently published ligand-based classifier based on the application of different machine learning algorithms was employed [55]. Importantly, none of the considered *Mab-SaS* inhibitors were predicted to be hERG blockers. Notably, all the compounds under investigation fall within the applicability domain of the model [56], thus confirming the reliability of the performed predictions.

3. Conclusions

The emergence of *Mab* as a dangerous pathogen for CF patients is becoming a worldwide health threat, due to its intrinsic resistance to several classes of antibiotics. For this reason, the aim of our research was to identify new compounds targeting the mycobacterial iron uptake, a crucial process during the infection, by inhibiting *Mab-SaS*.

To support the development of new *Mab-SaS* inhibitors and confirm the validity of the well-established 5-phenylfuran-2-carboxylic acid scaffold, we solved the crystal structure of the enzyme. Despite the overall conservation of the macromolecular architecture, key differences were detected between *Mab-SaS* and its *Mtb* ortholog, MbtI. Most notably, these discrepancies could explain the different biological performance of some compounds on the two enzymes. In this respect, we were able to identify a new promising furan-based inhibitor, exhibiting an IC_{50} in the low micromolar range. Incidentally, the compound was proven to be safe and demonstrated an excellent drug-likeness, estimated by *in-silico* calculations. These features confirmed the suitability of this inhibitor as a new lead for further studies on this chemical class and could enhance the speed and quality of drug design of improved compounds.

In conclusion, this work provides an important structural basis for the optimization of the known inhibitors and the computationally assisted development of new chemotypes targeting *Mab-SaS*, towards the design of new therapies for the treatment of *Mab* infections.

Table 4

X-ray data-collection and refinement statistics for *Mab-SaS*. Values in parentheses are for the highest resolution shell.

PDB_ID:	8QIJ
Space group	P2 ₁ 2 ₁ 2 ₁
Unit cell parameters	
<i>a</i> , <i>b</i> , <i>c</i> (Å)	94.34, 94.76, 102.46
α , β , γ (°)	90.0, 90.0, 90.0
Resolution (Å)	56.00–2.07 (2.11–2.07)
R _{merge}	0.186 (1.281)
R _{meas}	0.195 (1.340)
CC _{1/2}	0.997 (0.818)
$\langle I \rangle / \sigma(I)$	11.9 (2.2)
Completeness (%)	100.0 (100.0)
Total number unique observations	56395 (2794)
Redundancy	11.4 (11.7)
R _{work} /R _{free}	0.177/0.217
No. of refined atoms	
Protein	6641
Ligand/ion	91
Water	343
B factor (Å ²)	
Main chain	32.83
Side chain	35.86
Ligands	54.29
Water	37.18
R.m.s deviation	
Bond length (Å)	0.005
Bond angle (°)	1.217
Molprobrity - Ramachandran Plot	
Allowed regions (%)	97.93
Disallowed regions (%)	0.23

4. Materials and methods

4.1. Crystallization and crystal structure determination

Initial crystallization conditions were established using a 25 mg/mL purified sample of *Mab*-SaS by conducting a high-throughput screening, based on commercially available crystallization screens. Two promising conditions were identified: I) E9 from the Nextal Classic I suite (Qiagen, Hilden, Germany) and II) F6 from the Index suite (Hampton Research, Aliso Viejo, CA, USA). These conditions were then subjected to further optimization by exploring three different *Mab*-SaS concentrations: 8.5 mg/mL, 12 mg/mL, and 25 mg/mL. Crystals with a thin-rod shape were observed to develop in 3–4 weeks using the following precipitant composition for condition I: 0.75–0.95 M lithium sulfate, 0.45–0.55 M ammonium sulfate, and 0.1 M sodium citrate (pH 5.6). Crystals with a slightly thicker profile grew in nearly 3 months under condition II, which employed the following precipitant composition: 23%–27 % PEG 3350, 0.15–0.25 M ammonium sulfate, and 0.1 M BIS-TRIS (pH 5.5). The best quality crystals were obtained when using protein concentrations of 12 or 25 mg/mL. Both crystal forms were evaluated at the ELETTRA XRD2 beamline [57]. Crystals were cryopreserved by flash-freezing in liquid nitrogen using cryoprotectants composed of 80 % precipitant solution and 20 % glycerol. Data were collected at a temperature of 100 K and a wavelength of 1.00 Å, with a total rotation of 360°. Crystals grown under condition I diffracted to a maximum resolution of 2.53 Å, while crystals grown under condition II diffracted up to 2.07 Å. The subsequent analysis revealed them to be isomorphous. Data reduction was performed using Autoproc software [58] (details provided in Table 4); the structure solution was performed by molecular replacement using Phaser [59] and referencing the AlphaFold2 [60] model, available at the EBI database (<https://alphafold.ebi.ac.uk/entry/B1MAQ5>). Initial refinement steps were carried out using phenix.refine [61] for both crystal forms; no significant structural differences were detected between the two. However, crystal form II provided superior electron density maps, in accordance with the higher resolution of the data. As a result, the final structural refinement steps were performed exclusively for this dataset, using REFMAC [62]. Throughout the refinement process, manual rebuilding was conducted in tandem with COOT [63]. Analysis of the crystallographic structure and the preparation of model images for *Mab*-SaS were achieved using ChimeraX [64]. Sequence alignment representation was done by ESPript 3 package [9]. Data were validated and deposited with the Protein Data Bank (PDB) under the identifier 8QLJ.

4.2. *Mab*-SaS inhibition assays

Mab-SaS and *Mtb*-MbtI were expressed and purified to homogeneity by Immobilized Metal Affinity Chromatography and Gel Filtration, as previously reported [20,28]. Enzyme activity was determined by a fluorimetric assay [28] performed at 37 °C in 50 mM Hepes pH 7.5 and 5 mM MgCl₂, using 1–2 μM of enzymes. The reaction was started by the addition of chorismic acid and monitored in a PerkinElmer LS3 fluorimeter (Ex. λ = 305 nm, Em. λ = 420 nm; PerkinElmer, Waltham, MA, USA). Compound inhibition effects were determined at subsaturating concentrations of chorismic acid (50 μM) and at a fixed concentration of 100 μM. For compounds displaying a residual activity (%RA) below 30 % in the above conditions, the IC₅₀ value was determined by assaying the enzymatic activity at increasing compound concentrations (0.1–200 μM) and fitting the values according to equation (1) [65], with Graph-Pad Prism 8 software:

$$A_{[I]} = A_{[0]} * \left(1 - \frac{[I]}{[I] + IC_{50}} \right) \quad \text{Eq. 1}$$

where A_[I] is the enzyme activity in the presence of a given concentration of inhibitor [I], and A_[0] is the enzyme activity in the absence of

inhibitors.

4.3. Pan assay interference compounds (PAINS) analysis

In our previous works, we extensively demonstrated that the members of our furan-based library did not act as pan-assay interference compounds. To further verify the reliability of the inhibition results against *Mab*-SaS, we determined the IC₅₀ of compound **1h** in the presence of 0.1 mg/mL bovine serum albumin (BSA) or in the presence of 0.01 % (v/v) Triton X-100 as a detergent [28]. Moreover, to exclude an unspecific binding to cysteine residues, we also tested the IC₅₀ with 100 μM of 1,4-dithio-DL-threitol (DTT).

4.4. Cytotoxicity assays

Juvenile fibroblasts, isolated from human male foreskin, were kindly provided by Dr. M. Garofalo (Department of Pharmaceutical and Pharmacological Sciences, Padova, Italy). Cells were cultured in Dulbecco's Modified Eagle Medium (DMEM), 1 % L-glutamine (Gibco Laboratories, ThermoFisher Scientific, Waltham, MA, USA), 1 % penicillin/streptomycin (Gibco Laboratories), and 10 % fetal bovine serum (FBS, Gibco Laboratories). The cells were seeded at a density of 1 × 10⁴ cells/well in 96-well plates and maintained under standard growth conditions. After 24 h, cells were treated with **1h** at 0.5 μM, 1 μM, 5 μM, and 10 μM to a final volume of 100 μL. After 96 h, cell viability was assessed by MTS assay, according to the manufacturer's protocol (Cell Titer 96 Aqueous One Solution Cell Proliferation Assay; Promega, Naccka, Sweden) using a 96-well-plate spectrophotometer (Varioskan Flash Multimode Reader; ThermoFisher Scientific) set at λ = 490 nm. The absorbance value of untreated cells was set at 100 % (control), and the viability of treated cells was expressed as a percentage of the control. Three independent experiments were performed for each condition.

4.5. Chemistry

Starting reagents and solvents were acquired from commercial suppliers (Merck KGaA, Darmstadt, Germany; FluoroChem, Hadfield, UK) and used as received. All reactions were monitored by thin-layer chromatography (TLC), using aluminum-backed silica gel 60 plates (0.2 mm; Merck). Microwave-assisted reactions were carried out with a Biotage® Initiator Classic synthesizer (Biotage, Uppsala, Sweden). Crude products were purified by flash column chromatography on silica gel 60 (40–63 μM; Merck) using the indicated eluent system. Melting points were determined in open capillary tubes on a Stuart SMP30 Melting Point Apparatus (Cole-Parmer Stuart, Stone, UK). All tested compounds were characterized at T_{amb} by means of ¹H and ¹³C NMR spectroscopy on a Varian Oxford 300 MHz instrument (Varian, Palo Alto, CA, USA), operating at 300 MHz for ¹H and 75 MHz for ¹³C. Chemical shifts are expressed in ppm (δ), and J-couplings are given in Hertz. High-resolution mass spectrometry (HRMS) experiments were carried out on a Q-ToF Synapt G2-Si HDMS spectrometer (Waters, Milford, MA, USA). The purity of the tested compounds (≥95 %) was assessed by RP-HPLC on a Waters system, using a Phenomenex Luna® 3 μM C18(2) 100 Å, 4.6 × 100 mm column (Phenomenex, Torrance, CA, USA). The operative conditions for each compound are specified in the Supplementary Materials (SM). The preparation and characterization of compounds **1a-h,j-k** and **2** are described in our previous works [28,42], while the synthesis of **1i** and **3-5** is detailed in the next paragraphs, following the reaction steps illustrated in Schemes 1 and 2. Intermediates **6** and **7** were acquired from commercial sources, while **8** was prepared according to the procedure reported in the SM (Scheme S1) [66]. All the relevant spectra and chromatograms are listed in the SM.

4.5.1. Methyl 5-(3-sulfamoylphenyl)furan-2-carboxylate (4)

General Procedure A. Bis(triphenylphosphine)palladium(II)

dichloride (0.1 mmol), the appropriate boronic acid or boron pinacolate (1.3 mmol), and the suitable bromo-derivative (1.0 mmol) were transferred in a microwave tube under a nitrogen atmosphere. Dry 1,4-dioxane (3.5 mL) and a 2 M Na₂CO₃ (2 mmol, 0.85 mL) solution were added, and the mixture was stirred for 5 min at RT, and then in a microwave synthesizer for 70 min at 60 °C. The mixture was diluted with H₂O and extracted with EtOAc (3 x 10 mL). The organic layers were dried over anhydrous Na₂SO₄, filtered, and evaporated under reduced pressure. The crude product was purified by flash column chromatography to achieve the desired product. Starting compounds: (5-(methoxycarbonyl)furan-2-yl)boronic acid and 3-bromobenzenesulfonamide (6). Purification: flash column chromatography (cyclohexane/EtOAc 5:5). Yield: 77 %. Aspect: white solid. mp: 238 °C. TLC (cyclohexane/EtOAc 5:5): R_f = 0.38. ¹H NMR (300 MHz, Acetone-*d*₆) δ (ppm): 8.32 (t, *J* = 1.8 Hz, 1H, H_{Ar}), 8.06 (ddd, *J* = 7.8, 1.8, 1.1 Hz, 1H, H_{Ar}), 7.91 (ddd, *J* = 7.8, 1.8, 1.1 Hz, 1H, H_{Ar}), 7.69 (t, *J* = 7.8 Hz, 1H, H_{Ar}), 7.36 (d, *J* = 3.7 Hz, 1H, H_{Ar}), 7.21 (d, *J* = 3.7 Hz, 1H, H_{Ar}), 6.73 (br s exch. D₂O, 2H, SO₂NH₂), 3.90 (s, 3H, CH₃). ¹³C NMR (75 MHz, Acetone-*d*₆) δ (ppm): 158.31 (COOCH₃), 155.54 (C_{Ar}), 145.29 (C_{Ar}), 144.33 (C_{Ar}), 130.24 (C_{Ar}), 129.79 (C_{Ar}), 127.73 (C_{Ar}), 126.16 (C_{Ar}), 121.80 (C_{Ar}), 119.84 (C_{Ar}), 108.68 (C_{Ar}), 51.25 (COOCH₃). HRMS (ESI/Q-ToF): *m/z* calcd. for C₁₂H₁₀NO₅S 280.0280, found 280.0284.

4.5.2. Methyl 5-(3-(methylsulfonyl)phenyl)furan-2-carboxylate (9)

The compound was obtained according to General Procedure A. Starting compounds: (5-(methoxycarbonyl)furan-2-yl)boronic acid and 1-bromo-3-(methylsulfonyl)benzene (7). Purification: flash column chromatography (cyclohexane/EtOAc 6:4). Yield: 46 %. Aspect: greenish solid. mp: 163 °C. TLC (cyclohexane/EtOAc 6:4): R_f = 0.15. ¹H NMR (300 MHz, CDCl₃) δ (ppm): 8.31 (t, *J* = 1.8 Hz, 1H, H_{Ar}), 8.11–8.02 (m, 1H, H_{Ar}), 7.97–7.85 (m, 1H, H_{Ar}), 7.64 (t, *J* = 7.9 Hz, 1H, H_{Ar}), 7.28 (d, *J* = 3.6 Hz, 1H, H_{Ar}), 6.88 (d, *J* = 3.6 Hz, 1H, H_{Ar}), 3.94 (s, 3H, COOCH₃), 3.11 (s, 3H, SO₂CH₃).

4.5.3. Methyl 5-(2-sulfamoylphenyl)furan-2-carboxylate (10)

The compound was obtained according to General Procedure A. Starting compounds: (5-(methoxycarbonyl)furan-2-yl)boronic acid and 2-bromobenzenesulfonamide (8). Purification: flash column chromatography (cyclohexane/EtOAc 6:4). Yield: 14 %. Aspect: white solid. mp: 176 °C. TLC (cyclohexane/EtOAc 6:4): R_f = 0.34. ¹H NMR (300 MHz, CDCl₃) δ (ppm): 8.42–8.12 (m, 1H, H_{Ar}), 7.81–7.44 (m, 3H, H_{Ar}), 7.28–7.23 (m, partially overlapped with solvent peak, 1H, H_{Ar}), 6.78 (d, *J* = 3.6 Hz, 1H, H_{Ar}), 5.72 (br s exch. D₂O, 2H, SO₂NH₂), 3.93 (s, 3H, COOCH₃).

4.5.4. 5-(3-(Methylsulfonyl)phenyl)furan-2-carboxylic acid (1i)

General Procedure B. The suitable methyl ester (0.15 mmol) was dissolved in a 2:1 mixture of THF/H₂O (1 mL); then, LiOH·H₂O (0.38 mmol) was added after cooling to 0 °C. The reaction was stirred at the same temperature for some minutes, and then at room temperature for 4h. The solvent was evaporated under reduced pressure, maintaining the mixture at RT. The aqueous phase was acidified in an ice bath until pH 2–3 by adding a few drops of a 3 M HCl solution. The precipitate was recovered by filtration and washed with a few drops of a 6:4 solution of cyclohexane/EtOAc to yield the desired product. Starting compound: methyl 5-(3-(methylsulfonyl)phenyl)furan-2-carboxylate (9). Yield: 88 %. Aspect: greyish solid. mp: 226 °C. TLC (DCM/MeOH 9:1): R_f = 0.11. ¹H NMR (300 MHz, Acetone-*d*₆) δ (ppm): 11.60 (bs exch. D₂O, 1H, COOH), 8.37 (t, *J* = 1.7 Hz, 1H, H_{Ar}), 8.31–8.07 (m, 1H, H_{Ar}), 8.07–7.90 (m, 1H, H_{Ar}), 7.78 (t, *J* = 7.8 Hz, 1H, H_{Ar}), 7.38 (d, *J* = 3.7 Hz, 1H, H_{Ar}), 7.28 (d, *J* = 3.7 Hz, 1H, H_{Ar}), 3.21 (s, 3H, SO₂CH₃). ¹³C NMR (75 MHz, Acetone-*d*₆) δ (ppm): 158.90 (COOH), 155.10 (C_{Ar}), 144.96 (C_{Ar}), 142.52 (C_{Ar}), 130.74 (C_{Ar}), 130.19 (C_{Ar}), 129.11 (C_{Ar}), 127.24 (C_{Ar}), 123.02 (C_{Ar}), 119.95 (C_{Ar}), 109.12 (C_{Ar}), 43.32 (SO₂CH₃). HRMS (ESI/Q-ToF): *m/z* calcd. for C₁₂H₁₀O₅NaS 289.0147, found 289.0147.

4.5.5. 5-(2-Sulfamoylphenyl)furan-2-carboxylic acid (3)

The compound was obtained according to General Procedure B. Starting compound: methyl 5-(2-sulfamoylphenyl)furan-2-carboxylate (10). Yield: 70 %. Aspect: white solid. mp: 212 °C (dec.). TLC (DCM/MeOH 8:2): R_f = 0.37. ¹H NMR (300 MHz, Acetone-*d*₆) δ (ppm): 8.18 (dd, *J* = 7.9, 1.4 Hz, 1H, H_{Ar}), 7.84 (dd, *J* = 7.6, 1.5 Hz, 1H, H_{Ar}), 7.74 (td, *J* = 7.5, 1.4 Hz, 1H, H_{Ar}), 7.65 (td, *J* = 7.6, 1.5 Hz, 1H, H_{Ar}), 7.36 (d, *J* = 3.6 Hz, 1H, H_{Ar}), 7.06 (d, *J* = 3.6 Hz, 1H, H_{Ar}), 6.71 (br s exch. D₂O, 2H, SO₂NH₂). ¹³C NMR (75 MHz, Acetone-*d*₆) δ (ppm): 158.87 (COOH), 155.17 (C_{Ar}), 144.58 (C_{Ar}), 141.65 (C_{Ar}), 132.24 (C_{Ar}), 130.70 (C_{Ar}), 129.55 (C_{Ar}), 129.11 (C_{Ar}), 127.59 (C_{Ar}), 118.93 (C_{Ar}), 111.41 (C_{Ar}). HRMS (ESI/Q-ToF): *m/z* calcd. for C₁₁H₉NO₅NaS 290.0099, found 290.0108.

4.5.6. Methyl 3-(4,4,5,5-tetramethyl-1,3,2-dioxaborolan-2-yl)benzoate (11)

Methyl 3-bromobenzoate (250 mg, 1.16 mmol), bis(pinacolato)diboron (355 mg, 1.4 mmol), [1,1'-bis(diphenylphosphino)ferrocene] palladium(II) dichloride (95 mg, 0.12 mmol), and KOAc (683 mg, 7 mmol) were dissolved in dry DME (10 mL) in a microwave test tube under a nitrogen atmosphere. The reaction was stirred in a microwave synthesizer at 100 °C for 25 min. Then, the mixture was filtered on a celite pad, diluted with water, and extracted with EtOAc (3 x 10 mL). The unified organic layers were dried over anhydrous Na₂SO₄, filtered, and evaporated under reduced pressure. The product was not isolated, and the resulting brown solid was directly used in the next step without further purification. TLC (cyclohexane/EtOAc 7:3): R_f = 0.32.

4.5.7. Methyl 3'-sulfamoyl-[1,1'-biphenyl]-3-carboxylate (12)

The compound was obtained according to General Procedure A. Starting compounds: methyl 3-(4,4,5,5-tetramethyl-1,3,2-dioxaborolan-2-yl)benzoate (11) and 3-bromobenzenesulfonamide (6). Purification: flash column chromatography (cyclohexane/EtOAc 6:4). Yield: 40 %. Aspect: white solid. mp: 152 °C. TLC (cyclohexane/EtOAc 6:4): R_f = 0.15. ¹H NMR (300 MHz, CDCl₃) δ (ppm): 8.28 (t, *J* = 1.7 Hz, 1H, H_{Ar}), 8.18 (t, *J* = 1.7 Hz, 1H, H_{Ar}), 8.11–8.05 (m, 1H, H_{Ar}), 7.99–7.91 (m, 1H, H_{Ar}), 7.88–7.77 (m, 2H, H_{Ar}), 7.62 (t, *J* = 7.8 Hz, 1H, H_{Ar}), 7.56 (t, *J* = 7.8 Hz, 1H, H_{Ar}), 4.91 (br s exch. D₂O, 2H, SO₂NH₂), 3.96 (s, 3H, COOCH₃).

4.5.8. 3'-Sulfamoyl-[1,1'-biphenyl]-3-carboxylic acid (5)

The compound was obtained according to General Procedure B. Starting compound: methyl 3'-sulfamoyl-[1,1'-biphenyl]-3-carboxylate (12). Reaction time: 6 h. Yield: 92 %. Aspect: white solid. mp: 202 °C (dec.). TLC (DCM/MeOH 8:2): R_f = 0.45. ¹H NMR (300 MHz, acetone-*d*₆) δ (ppm): 8.35 (t, *J* = 1.7 Hz, 1H, H_{Ar}), 8.27 (t, *J* = 1.8 Hz, 1H, H_{Ar}), 8.09 (dt, *J* = 7.7, 1.3 Hz, 1H, H_{Ar}), 8.00 (ddd, *J* = 7.8, 1.9, 1.1 Hz, 1H), 7.96 (dt, *J* = 2.8, 1.1 Hz, 1H), 7.95–7.93 (m, 1H), 7.70 (t, *J* = 7.8 Hz, 1H), 7.66 (t, *J* = 7.8 Hz, 1H, H_{Ar}), 6.80 (br s exch. D₂O, 2H, SO₂NH₂). ¹³C NMR (75 MHz, acetone-*d*₆) δ (ppm): 167.33 (COOH), 145.14 (C_{Ar}), 140.67 (C_{Ar}), 139.79 (C_{Ar}), 131.56 (C_{Ar}), 131.47 (C_{Ar}), 130.26 (C_{Ar}), 129.68 (C_{Ar}), 129.40 (C_{Ar}), 129.16 (C_{Ar}), 127.95 (C_{Ar}), 125.21 (C_{Ar}), 124.52 (C_{Ar}). HRMS (ESI/Q-ToF): *m/z* calcd. for C₁₃H₁₀NO₄S 276.0331, found 276.0334.

4.6. Molecular docking simulations

First, **1f**, **1h**, **1i**, and **1k** were docked in the binding site of the solved X-ray *Mab*-SaS structure using Grid-based Ligand Docking with Energetics (GLIDE) as software [67]. X-ray *Mab*-SaS was prepared using the protein preparation wizard workflow [68], which enabled us to (i) add missing hydrogen atoms, (ii) determine the optimal protonation and tautomerization states of the residues, (iii) fix the orientation of any misoriented group, and (iv) perform a final energy minimization. All the ligands were prepared using LigPrep [69] to generate all the possible tautomers and ionization states at pH 7.0 ± 2.0. Induced Fit Docking

(IFD) simulations were performed with the SP mode and all default settings to account for putative conformational rearrangements within the protein binding site during molecular recognition [70]. The binding site of the X-ray *Mab*-SaS structure was identified by superimposing the homology model built in our previous study [20]. This was accomplished using the Superposition tool available from the Schrödinger suite 2022–4, yielding an RMSD of 6.05 Å. Subsequently, a cubic grid was created, centered on the cognate ligand of the homology model (coordinates: $x = 7.24$, $y = 12.25$, $z = 8.87$). The grid comprised an inner box measuring $10 \text{ \AA} \times 10 \text{ \AA} \times 10 \text{ \AA}$ and an outer box of $24 \text{ \AA} \times 24 \text{ \AA} \times 24 \text{ \AA}$. The top-scored complex of **1h** was used as a starting point for performing docking simulations on the analogs **2**, **3**, **4**, and **5**. Specifically, a cubic grid centered on **1h** with an inner box size of $10 \text{ \AA} \times 10 \text{ \AA} \times 10 \text{ \AA}$ and an outer box size of $23 \text{ \AA} \times 23 \text{ \AA} \times 23 \text{ \AA}$ was utilized. These docking simulations were conducted using the SP mode, increasing both the number of generated poses per ligand (from 5000, the default setting, to 50,000) and the number retained for energy minimization (from 400, the default setting, to 4000). Conformational space exploration was constrained to ensure that only poses consistent with the coordinates of **1h** (with a tolerance of 2.0 Å) were considered. The protocol was validated by docking **1h**, yielding an RMSD = 0.40 Å.

4.7. MM-GBSA calculations

All top-scored docking complexes underwent molecular mechanics/generalized Born surface area (MM-GBSA) calculations to determine their respective ligand-protein binding free energies (ΔG) [71]. More negative ΔG values indicate stronger binding affinities. These calculations were conducted using Prime, with the default dielectric constants, the OPLS4 [72] force field, and the VSGB solvation model. Notably, no flexibility was permitted for the residues within the protein cavity during these calculations. This decision was made based on the consideration that conformational rearrangements of the binding site had already been accounted for during the IFD simulations.

Notes

The authors declare no competing financial interest.

Authors will release the atomic coordinates and experimental data upon article publication.

CRediT authorship contribution statement

Matteo Mori: Investigation, Writing – original draft, Writing – review & editing. **Mario Cocorullo:** Investigation. **Andrea Tresoldi:** Investigation. **Giulia Cazzaniga:** Investigation. **Arianna Gelain:** Investigation. **Giovanni Stelitano:** Investigation. **Laurent R. Chiarelli:** Conceptualization, Writing – original draft, Writing – review & editing, Funding acquisition, Supervision. **Martina Tomaiuolo:** Investigation. **Pietro Delre:** Investigation. **Giuseppe F. Mangiatordi:** Conceptualization, Writing – original draft, Writing – review & editing. **Mariangela Garofalo:** Investigation. **Alberto Cassetta:** Investigation, Writing – original draft, Writing – review & editing. **Sonia Covaceuszach:** Conceptualization, Funding acquisition, Supervision, Writing – original draft, Writing – review & editing. **Stefania Villa:** Conceptualization, Funding acquisition, Supervision, Writing – original draft, Writing – review & editing. **Fiorella Meneghetti:** Conceptualization, Funding acquisition, Supervision, Writing – original draft, Writing – review & editing.

Declaration of competing interest

The authors declare the following financial interests/personal relationships which may be considered as potential competing interests: Laurent R. Chiarelli reports financial support was provided by Italian Cystic Fibrosis Research Foundation (FFC Ricerca). If there are other

authors, they declare that they have no known competing financial interests or personal relationships that could have appeared to influence the work reported in this paper.

Data availability

Data will be made available on request.

Acknowledgments

The authors would like to thank Fondazione Ricerca Fibrosi Cistica Onlus and the supporting groups that adopted the project (FFC#5–2022): Gruppo di sostegno FFC Ricerca “Miriam Colombo”—Ospedaletti; Gruppo di sostegno FFC Ricerca di Grado—Gorizia; Gruppo di sostegno FFC Ricerca di Benevento; Delegazione FFC Ricerca di Monterotondo Roma; Delegazione FFC Ricerca di Vigevano; Delegazione FFC Ricerca di Trieste; Delegazione FFC Ricerca di Sassari Castelsardo; Delegazione FFC Ricerca di Moncalvo; Delegazione FFC Ricerca di Lecce. Moreover, the authors acknowledge the Mass Spectrometry Facility of the Unitech COSPECT at the University of Milan (Italy) for the HRMS analyses.

Appendix A. Supplementary data

Supplementary data to this article can be found online at <https://doi.org/10.1016/j.ejmech.2023.116073>.

References

- [1] H.F.M. Abdelaal, E.D. Chan, L. Young, S.L. Baldwin, R.N. Coler, *Mycobacterium abscessus*: it's Complex, *Microorganisms* 10 (2022) 1454, <https://doi.org/10.3390/MICROORGANISMS10071454>.
- [2] K.L. Winthrop, T.K. Marras, J. Adjemian, H. Zhang, P. Wang, Q. Zhang, Incidence and prevalence of nontuberculous mycobacterial lung disease in a large U.S. managed care health plan, 2008–2015, *Ann. Am. Thorac. Soc.* 17 (2020) 178–185, <https://doi.org/10.1513/ANNALSATS.201804-236OC>.
- [3] M.D. Johansen, J.L. Herrmann, L. Kremer, Non-tuberculous mycobacteria and the rise of *Mycobacterium abscessus*, *Nat. Rev. Microbiol.* 18 (2020) 392–407, <https://doi.org/10.1038/s41579-020-0331-1>.
- [4] J.R. Sullivan, A. Lupien, E. Kalthoff, C. Hamela, L. Taylor, K.A. Munro, T. M. Schmeing, L. Kremer, M.A. Behr, Efficacy of eptaborole against *Mycobacterium abscessus* is increased with norvaline, *PLoS Pathog.* 17 (2021), e1009965, <https://doi.org/10.1371/JOURNAL.PPAT.1009965>.
- [5] V.A. Kelley, J.S. Schorey, *Mycobacterium*'s arrest of phagosome maturation in macrophages requires Rab5 activity and accessibility to iron, *Mol. Biol. Cell* 14 (2003) 3366–3377, <https://doi.org/10.1091/MBE.E02-12-0780>.
- [6] C. Cristancho-Rojas, C.D. Varley, S.C. Lara, Y. Kherabi, E. Henkle, K.L. Winthrop, Epidemiology of *Mycobacterium abscessus*, *Clin. Microbiol. Infect.* (2023), <https://doi.org/10.1016/j.cmi.2023.08.035>.
- [7] C. Ruis, J.M. Bryant, S.C. Bell, R. Thomson, R.M. Davidson, N.A. Hasan, J. Van Ingen, M. Strong, R.A. Floto, J. Parkhill, Dissemination of *Mycobacterium abscessus* via global transmission networks, *Nat. Microbiol.* 6 (2021) 1279–1288, <https://doi.org/10.1038/s41564-021-00963-3>.
- [8] L. Victoria, A. Gupta, J.L. Gómez, J. Robledo, *Mycobacterium abscessus* complex: a review of recent developments in an emerging pathogen, *Front. Cell. Infect. Microbiol.* 11 (2021), 659997, <https://doi.org/10.3389/FCIMB.2021.659997>.
- [9] Y. Vande Weygaerde, N. Cardinaels, P. Bomans, T. Chin, J. Boelens, E. André, E. Van Braeckel, N. Lorent, Clinical relevance of pulmonary non-tuberculous mycobacterial isolates in three reference centres in Belgium: a multicentre retrospective analysis, *BMC Infect. Dis.* 19 (2019) 1061, <https://doi.org/10.1186/S12879-019-4683-Y>.
- [10] I.K. Park, K.N. Olivier, Nontuberculous mycobacteria in cystic fibrosis and non-cystic fibrosis bronchiectasis, *Semin. Respir. Crit. Care Med.* 36 (2015) 217–224, <https://doi.org/10.1055/S-0035-1546751>.
- [11] D. Recchia, G. Stelitano, A. Stamilla, D.L. Gutierrez, G. Degiacomi, L.R. Chiarelli, M.R. Pasca, *Mycobacterium abscessus* infections in cystic fibrosis individuals: a review on therapeutic options, *Int. J. Mol. Sci.* 24 (2023) 4635, <https://doi.org/10.3390/IJMS24054635>.
- [12] D.E. Griffith, C.L. Daley, Treatment of *Mycobacterium abscessus* pulmonary disease, *Chest* 161 (2022) 64–75, <https://doi.org/10.1016/J.CHEST.2021.07.035>.
- [13] S.E. Mudde, J.A. Schildkraut, N.C. Ammerman, C.P. de Vogel, J.E.M. de Steenwinkel, J. van Ingen, H.I. Bax, Unraveling antibiotic resistance mechanisms in *Mycobacterium abscessus*: the potential role of efflux pumps, *J. Glob. Antimicrob. Resist.* 31 (2022) 345–352, <https://doi.org/10.1016/J.JGAR.2022.10.015>.
- [14] M.L. Wu, D.B. Aziz, V. Dartois, T. Dick, NTM drug discovery: status, gaps and the way forward, *Drug Discov. Today* 23 (2018) 1502, <https://doi.org/10.1016/J.DRUDIS.2018.04.001>.

- [15] C. Pecoraro, D. Carbone, D. Deng, S.M. Cascioferro, P. Diana, E. Giovannetti, Biofilm Formation as valuable target to fight against severe chronic infections, *Curr. Med. Chem.* 29 (2022) 4307–4310, <https://doi.org/10.2174/0929867329666220103095551>.
- [16] M. Meir, D. Barkan, Molecular sciences alternative and experimental therapies of *Mycobacterium abscessus* infections, *Int. J. Mol. Sci.* 21 (2020) 6793, <https://doi.org/10.3390/ijms21186793>.
- [17] I. Palucci, G. Delogu, Alternative therapies against *Mycobacterium abscessus* infections, *Clin. Microbiol. Infect.* (2023), <https://doi.org/10.1016/j.cmi.2023.10.001>.
- [18] S. Ahmed, M.Z. Ahmed, S. Rafique, S.E. Almasoudi, M. Shah, N.A.C. Jalil, S. C. Ojha, Recent approaches for downplaying antibiotic resistance: molecular mechanisms, *BioMed Res. Int.* 2023 (2023), 5250040, <https://doi.org/10.1155/2023/5250040>.
- [19] A. Tarín-Pelló, B. Suay-García, M.T. Pérez-Gracia, Antibiotic resistant bacteria: current situation and treatment options to accelerate the development of a new antimicrobial arsenal, *Expert Rev. Anti Infect. Ther.* 20 (2022) 1095–1108, <https://doi.org/10.1080/14787210.2022.2078308>.
- [20] M. Mori, G. Stelitano, G. Cazzaniga, A. Gelain, A. Tresoldi, M. Cocorullo, M. Roversi, L.R. Chiarelli, M. Tomaiuolo, P. Delre, G.F. Mangiatordi, A. Griego, L. Rizzello, A. Cassetta, S. Covaceuszach, S. Villa, F. Meneghetti, Targeting siderophore-mediated iron uptake in *M. abscessus*: a new strategy to limit the virulence of non-tuberculous mycobacteria, *Pharmaceutics* 15 (2023) 502, <https://doi.org/10.3390/PHARMACEUTICS15020502>.
- [21] M. Nairz, G. Weiss, Iron in infection and immunity, *Mol. Aspects Med.* 75 (2020), 100864, <https://doi.org/10.1016/j.mam.2020.100864>.
- [22] E.E. Johnson, M. Wessling-Resnick, Iron metabolism and the innate immune response to infection, *Microb. Infect.* 14 (2012) 207–216, <https://doi.org/10.1016/j.micinf.2011.10.001>.
- [23] A. Chao, P.J. Sieminski, C.P. Owens, C.W. Goulding, Iron acquisition in *Mycobacterium tuberculosis*, *Chem. Rev.* 119 (2019) 1193–1220, <https://doi.org/10.1021/acs.chemrev.8b00285>.
- [24] G.V. Bythrow, M.F. Farhat, K. Levendosky, P. Mohandas, G.A. Germain, B. Yoo, L. E.N. Quadri, *Mycobacterium abscessus* mutants with a compromised functional link between the type VII ESX-3 system and an iron uptake mechanism reliant on an unusual mycobactin siderophore, *Pathogens* 11 (2022) 953, <https://doi.org/10.3390/pathogens11090953>.
- [25] M. Foreman, I. Kolodkin-Gal, D. Barkan, A pivotal role for mycobactin/mbtE in growth and adaptation of *Mycobacterium abscessus*, *Microbiol. Spectr.* 10 (2022), e02623, <https://doi.org/10.1128/spectrum.02623-22>.
- [26] M. Shyam, D. Shilkar, G. Rakshit, V. Jayaprakash, Approaches for targeting the mycobactin biosynthesis pathway for novel anti-tubercular drug discovery: where we stand, *Expert Opin. Drug Discov.* 17 (2022) 699–715, <https://doi.org/10.1080/17460441.2022.2077328>.
- [27] G. Stelitano, M. Cocorullo, M. Mori, S. Villa, F. Meneghetti, L.R. Chiarelli, Iron acquisition and metabolism as a promising target for antimicrobials (bottlenecks and opportunities): where do we stand? *Int. J. Mol. Sci.* 24 (2023) 6181, <https://doi.org/10.3390/IJMS24076181>.
- [28] M. Mori, G. Stelitano, A. Gelain, E. Pini, L.R. Chiarelli, J.C. Sammartino, G. Poli, T. Tuccinardi, G. Beretta, A. Porta, M. Bellinzoni, S. Villa, F. Meneghetti, Shedding X-ray light on the role of magnesium in the activity of *M. tuberculosis* salicylate synthase (MbtI) for drug design, *J. Med. Chem.* 63 (2020) 7066–7080, <https://doi.org/10.1021/acs.jmedchem.0c00373>.
- [29] F. Hubrich, M. Müller, J.N. Anderer, Chorismate- and isochorismate converting enzymes: versatile catalysts acting on an important metabolic node, *Chem. Commun.* 57 (2021) 2441–2463, <https://doi.org/10.1039/D0CC08078K>.
- [30] C.L. Shelton, A.L. Lamb, Unraveling the structure and mechanism of the MST(ery) enzymes, *Trends Biochem. Sci.* 43 (2018) 342–357, <https://doi.org/10.1016/j.tibs.2018.02.011>.
- [31] A. Manos-Turvey, K.M. Cergol, N.K. Salam, E.M.M. Bulloch, G. Chi, A. Pang, W. J. Britton, N.P. West, E.N. Baker, J.S. Lott, R.J. Payne, Synthesis and evaluation of *M. tuberculosis* salicylate synthase (MbtI) inhibitors designed to probe plasticity in the active site, *Org. Biomol. Chem.* 10 (2012) 9223–9236, <https://doi.org/10.1039/C2OB26736E>.
- [32] M.D. Winn, C.C. Ballard, K.D. Cowtan, E.J. Dodson, P. Emsley, P.R. Evans, R. M. Keegan, E.B. Krissinel, A.G.W. Leslie, A. McCoy, S.J. McNicholas, G. N. Murshudov, N.S. Pannu, E.A. Potterton, H.R. Powell, R.J. Read, A. Vagin, K. S. Wilson, IUCr, Overview of the CCP 4 suite and current developments, *Acta Crystallogr. Sect. D Biol. Crystallogr.* 67 (2011) 235–242, <https://doi.org/10.1107/S0907444910045749>.
- [33] A.J. Harrison, M. Yu, T. Gårdenborg, M. Middleditch, R.J. Ramsay, E.N. Baker, J. S. Lott, The structure of MbtI from *Mycobacterium tuberculosis*, the first enzyme in the biosynthesis of the siderophore mycobactin, reveals it to be a salicylate synthase, *J. Bacteriol.* 188 (2006) 6081–6091, <https://doi.org/10.1128/JB.00338-06>.
- [34] G. Chi, A. Manos-Turvey, P.D. O'Connor, J.M. Johnston, G.L. Evans, E.N. Baker, R. J. Payne, J.S. Lott, E.M.M. Bulloch, Implications of binding mode and active site flexibility for inhibitor potency against the salicylate synthase from *Mycobacterium tuberculosis*, *Biochemistry* 51 (2012) 4868–4879, <https://doi.org/10.1021/bi3002067>.
- [35] O. Kerbarh, D.Y. Chirgadze, T.L. Blundell, C. Abell, Crystal structures of *Yersinia enterocolitica* salicylate synthase and its complex with the reaction products salicylate and pyruvate, *J. Mol. Biol.* 357 (2006) 524–534, <https://doi.org/10.1016/j.jmb.2005.12.078>.
- [36] G. Spraggon, C. Kim, X. Nguyen-Huu, M.C. Yee, C. Yanofsky, S.E. Mills, The structures of anthranilate synthase of *Serratia marcescens* crystallized in the presence of (i) its substrates, chorismate and glutamine, and a product, glutamate, and (ii) its end-product inhibitor, l-tryptophan, *Proc. Natl. Acad. Sci. USA* 98 (2001) 6021–6026, <https://doi.org/10.1073/pnas.111150298>.
- [37] J.F. Parsons, P.Y. Jensen, A.S. Pachikara, A.J. Howard, E. Eisenstein, J.E. Ladner, Structure of *Escherichia coli* aminodeoxychorismate synthase: architectural conservation and diversity in chorismate-utilizing enzymes, *Biochemistry* 41 (2002) 2198–2208, <https://doi.org/10.1021/B1015791B>.
- [38] D. Sehnal, R.S. Vařeková, K. Berka, L. Pravda, V. Navrátilová, P. Banáš, C. M. Ionescu, M. Otyepka, J. Koča, Mole 2.0: advanced approach for analysis of biomacromolecular channels, *J. Cheminf.* 5 (2013) 39, <https://doi.org/10.1186/1758-2946-5-39>.
- [39] A. Manos-Turvey, E.M.M. Bulloch, P.J. Rutledge, E.N. Baker, J.S. Lott, R.J. Payne, Inhibition studies of *Mycobacterium tuberculosis* salicylate synthase (MbtI), *ChemMedChem* 5 (2010) 1067–1079, <https://doi.org/10.1002/cmdc.201000137>.
- [40] R.A. Lee, M. Razaz, S. Hayward, The DynDom database of protein domain motions, *Bioinformatics* 19 (2003) 1290–1291, <https://doi.org/10.1093/BIOINFORMATICS/BTG137>.
- [41] J.L. Dahlin, J.W.M. Nissink, J.M. Strasser, S. Francis, L. Higgins, H. Zhou, Z. Zhang, L.R. Chiarelli, M. Mori, D. Barlocco, G. Beretta, A. Gelain, E. Pini, M. Porcino, G. Mori, G. Stelitano, L. Costantino, M. Lapillo, D. Bonanni, G. Poli, T. Tuccinardi, S. Villa, F. Meneghetti, Discovery and development of novel salicylate synthase (MbtI) furanic inhibitors as antitubercular agents, *Eur. J. Med. Chem.* 155 (2018) 754–763, <https://doi.org/10.1016/j.ejmech.2018.06.033>.
- [42] M. Mori, G. Stelitano, A. Griego, L.R. Chiarelli, G. Cazzaniga, A. Gelain, E. Pini, M. Camera, P. Canzano, A. Fumagalli, E. Scarpa, C. Cordiglieri, L. Rizzello, S. Villa, F. Meneghetti, Synthesis and assessment of the in vitro and ex vivo activity of salicylate synthase (MbtI) inhibitors as new candidates for the treatment of mycobacterial infections, *Pharmaceutics* 15 (2022) 992, <https://doi.org/10.3390/ph15080992>.
- [43] L.R. Chiarelli, M. Mori, G. Beretta, A. Gelain, E. Pini, J.C. Sammartino, G. Stelitano, D. Barlocco, L. Costantino, M. Lapillo, G. Poli, I. Caligiuri, F. Rizzolio, M. Bellinzoni, T. Tuccinardi, S. Villa, F. Meneghetti, New insight into structure-activity of furan-based salicylate synthase (MbtI) inhibitors as potential antitubercular agents, *J. Enzym. Inhib. Med. Chem.* 34 (2019) 823–828, <https://doi.org/10.1080/14756366.2019.1589462>.
- [44] J. Vrbanc, R. Slauter, ADME in drug discovery, in: *A Compr. Guid. To Toxicol. Nonclinical Drug Dev.*, Academic Press, 2017, pp. 39–67, <https://doi.org/10.1016/B978-0-12-803620-4.00003-7>.
- [45] G.R. Bickerton, G.V. Paolini, J. A. Besnard, S. Muresan, A.L. Hopkins, Quantifying the chemical beauty of drugs, *Nat. Chem.* 4 (2012) 90, <https://doi.org/10.1038/NCHEM.1243>.
- [46] M.R. Lee, W.H. Sheng, C.C. Hung, C.J. Yu, L.N. Lee, P.R. Hsueh, *Mycobacterium abscessus* complex infections in humans, *Emerg. Inf. Disp.* 21 (2015) 1638–1646, <https://doi.org/10.3201/EID2109.141634>.
- [47] W. Manjeese, N.E. Mvubu, A.J.C. Steyn, T. Mpfana, *Mycobacterium tuberculosis* causes a leaky blood-brain barrier and neuroinflammation in the prefrontal cortex and cerebellum regions of infected mice offspring, *Int. J. Dev. Neurosci.* 81 (2021) 428–437, <https://doi.org/10.1002/JDN.10116>.
- [48] Schrödinger Release 2022-4: QikProp, Schrödinger, LLC, New York, NY, USA, 2022.
- [49] W.L. Jorgensen, Efficient drug lead discovery and optimization, *Acc. Chem. Res.* 42 (2009) 724–733, <https://doi.org/10.1021/AR800236T>.
- [50] S. Tian, Y. Djoumbou-Feunang, R. Greiner, D.S. Wishart, CypReact: a software tool for in silico reactant prediction for human cytochrome P450 enzymes, *J. Chem. Inf. Model.* 58 (2018) 1282–1291, <https://doi.org/10.1021/ACS.JCIM.8B00035>.
- [51] T.M. Creanza, G. Lamanna, P. Delre, M. Contino, N. Corriero, M. Saviano, G. F. Mangiatordi, N. Ancona, DeLa-Drug: a deep learning algorithm for automated design of druglike analogues, *J. Chem. Inf. Model.* 62 (2022) 1411–1424, <https://doi.org/10.1021/ACS.JCIM.2C00205>.
- [52] T.M. Creanza, P. Delre, N. Ancona, G. Lentini, M. Saviano, G.F. Mangiatordi, Structure-Based prediction of hERG-related cardiotoxicity: a benchmark study, *J. Chem. Inf. Model.* 61 (2021) 4758–4770, <https://doi.org/10.1021/acs.jcim.1c00744>.
- [53] J.V. Phillely, M.A. DeGroot, J.R. Honda, M.M. Chan, S. Kasperbauer, N.D. Walter, E.D. Chan, Treatment of non-tuberculous mycobacterial lung disease, *Curr. Treat. Options Infect. Dis.* 8 (2016) 275–296, <https://doi.org/10.1007/S40506-016-0086-4>.
- [54] P. Delre, G.J. Lavado, G. Lamanna, M. Saviano, A. Roncaglioni, E. Benfenati, G. F. Mangiatordi, D. Gadaleta, Ligand-based prediction of hERG-mediated cardiotoxicity based on the integration of different machine learning techniques, *Front. Pharmacol.* 13 (2022), 951083, <https://doi.org/10.3389/FPHAR.2022.951083>.
- [55] D. Gadaleta, G.F. Mangiatordi, M. Catto, A. Carotti, O. Nicolotti, Applicability domain for QSAR models: where theory meets reality, *Int. J. Quant. Struct. Relationships.* 1 (2016) 45–63, <https://doi.org/10.4018/IJQSPR.2016010102>.
- [56] A. Lausi, M. Polentarutti, S. Onesti, J.R. Plaisier, E. Busetto, G. Bais, L. Barba, A. Cassetta, G. Campi, D. Lamba, A. Pifferi, S.C. Mande, D.D. Sarma, S.M. Sharma, G. Paolucci, Status of the crystallography beamlines at Elettra, *Eur. Phys. J. Plus.* 130 (2015) 43, <https://doi.org/10.1140/epjp/i2015-15043-3>.
- [57] C. Vonnhein, C. Flensburg, P. Keller, A. Sharff, O. Smart, W. Paciorek, T. Womack, G. Bricogne, Data processing and analysis with the autoPROC toolbox, *Acta Crystallogr. Sect. D Biol. Crystallogr.* 67 (2011) 293–302, <https://doi.org/10.1107/S0907444911007773>.

- [59] A.J. McCoy, R.W. Grosse-Kunstleve, P.D. Adams, M.D. Winn, L.C. Storoni, R. J. Read, *Phaser* crystallographic software, *J. Appl. Crystallogr.* 40 (2007) 658–674, <https://doi.org/10.1107/S0021889807021206>.
- [60] J. Jumper, R. Evans, A. Pritzel, T. Green, M. Figurnov, O. Ronneberger, K. Tunyasuvunakool, R. Bates, A. Židek, A. Potapenko, A. Bridgland, C. Meyer, S.A. Kohl, A.J. Ballard, A. Cowie, B. Romera-Paredes, S. Nikolov, R. Jain, J. Adler, T. Back, S. Petersen, D. Reiman, E. Clancy, M. Zielinski, M. Steinegger, M. Pacholska, T. Berghammer, S. Bodenstein, D. Silver, O. Vinyals, A.W. Senior, K. Kavukcuoglu, P. Kohli, D. Hassabis, Highly accurate protein structure prediction with AlphaFold, *Nature* 596 (2021) 583, <https://doi.org/10.1038/S41586-021-03819-2>.
- [61] P. V Afonine, R.W. Grosse-Kunstleve, N. Echols, J.J. Headd, N.W. Moriarty, M. Mustyakimov, T.C. Terwilliger, A. Urzhumtsev, P.H. Zwart, P.D. Adams, Towards automated crystallographic structure refinement with phenix.refine, *Acta Crystallogr. Sect. D Struct. Biol.* 68 (2012) 352–367, <https://doi.org/10.1107/S0907444912001308>.
- [62] G.N. Murshudov, A.A. Vagin, E.J. Dodson, Refinement of macromolecular structures by the maximum-likelihood method, *Acta Crystallogr. Sect. D Struct. Biol.* 53 (1997) 240–255, <https://doi.org/10.1107/S0907444996012255>.
- [63] P. Emsley, K. Cowtan, *Coot* : model-building tools for molecular graphics, *Acta Crystallogr. Sect. D Biol. Crystallogr.* 60 (2004) 2126–2132, <https://doi.org/10.1107/S0907444904019158>.
- [64] E.C. Meng, T.D. Goddard, E.F. Pettersen, G.S. Couch, Z.J. Pearson, J.H. Morris, T. E. Ferrin, UCSF ChimeraX: tools for structure building and analysis, *Protein Sci.* 32 (2023), e4792, <https://doi.org/10.1002/PRO.4792>.
- [65] R.A. Copeland, *Enzymes: A Practical Introduction to Structure, Mechanism and Data Analysis*, second ed., John Wiley & Sons Inc., New York, NY, USA, 2000.
- [66] G. Tang, X. Lin, Z. Qiu, W. Li, L. Zhu, L. Wang, S. Li, H. Li, W. Lin, M. Yang, T. Guo, L. Chen, D. Lee, J.Z. Wu, W. Yang, Design and synthesis of benzenesulfonamide derivatives as potent anti-influenza hemagglutinin inhibitors, *ACS Med. Chem. Lett.* 2 (2011) 603–607, <https://doi.org/10.1021/ML2000627>.
- [67] R.A. Friesner, R.B. Murphy, M.P. Repasky, L.L. Frye, J.R. Greenwood, T.A. Halgren, P.C. Sanschagrin, D.T. Mainz, Extra precision glide: docking and scoring incorporating a model of hydrophobic enclosure for protein-ligand complexes, *J. Med. Chem.* 49 (2006) 6177–6196, <https://doi.org/10.1021/jm051256o>.
- [68] Schrödinger Release 2022-4: Protein Preparation Wizard, Schrödinger LLC, New York, NY, USA, 2022.
- [69] Schrödinger Release 2022-4, LigPrep, Schrödinger LLC, New York, NY, USA, 2022.
- [70] Schrödinger Release 2022-4: Induced Fit Docking Protocol, Schrödinger, LLC, New York, NY, USA, 2022.
- [71] S. Genheden, U. Ryde, The MM/PBSA and MM/GBSA methods to estimate ligand-binding affinities, *Expert Opin. Drug Discov.* 10 (2015) 449–461, <https://doi.org/10.1517/17460441.2015.1032936>.
- [72] C. Lu, C. Wu, D. Ghoreishi, W. Chen, L. Wang, W. Damm, G.A. Ross, M.K. Dahlgren, E. Russell, C.D. Von Bargen, R. Abel, R.A. Friesner, E.D. Harder, OPLS4: improving force field accuracy on challenging regimes of chemical space, *J. Chem. Theory Comput.* 17 (2021) 4291–4300, <https://doi.org/10.1021/ACS.JCTC.1C00302>.